Research Square

Preprints are preliminary reports that have not undergone peer review.
They should not be considered conclusive, used to inform clinical practice,
or referenced by the media as validated information.

Multimodal imaging links iron, microglial dysfunction and lipid peroxidation in ALSP white matter

Nikita Ollen-Bittle
Western University
Bradley Karat
Western University
Qi Zhang
Western University
Robert Hammond
Western University
C. Dirk Keene
University of California San Diego Medical Center
Ali Khan
Western University
Elizabeth Finger
Western University
Shawn N. Whitehead
shawn.whitehead@schulich.uwo.ca

Western University https://orcid.org/0000-0003-4728-8067

Research Article

Keywords: ALSP, microglia, OxPC, lipids, white matter hyperintensity, iron

Posted Date: November 25th, 2026

DOI: https://doi.org/10.21203/rs.3.rs-11857701/v1

License: This work is licensed under a Creative Commons Attribution 4.0 International License.
Read Full License

Additional Declarations:
The authors declare no competing interests.

Tables 1 to 4 are available in the Supplementary Files section.

Multimodal imaging links iron, microglial dysfunction and lipid peroxidation in ALSP white matter

N. Ollen-Bittle[1], B. Karat[2], Q. Zhang[3,4], R. Hammond[3,4], C. Dirk Keene[5], A. R. Khan[2], E. Finger[3,6], S.N. Whitehead[1]

1 Department of Anatomy and Cell Biology, Schulich School of Medicine and Dentistry, Western University, London, ON, Canada.
2 Department of Medical Biophysics, The Schulich School of Medicine and Dentistry, The University of Western Ontario, London, ON, Canada.
3 Department of Clinical Neurological Sciences, Schulich School of Medicine and Dentistry, Western University, London, ON, Canada.
4 Department of Pathology and Laboratory Medicine, London Health Sciences Centre, London, ON, Canada.
5 Department of Pathology, University of California San Diego, La Jollam, CA, USA.
6 Department of Neurology, London Health Sciences Centre, London, ON, Canada

Ethics approval and previous publications: Informed consent was obtained for all specimens, according to the Declaration of Helsinki. All research was conducted under research ethics board approval under Western Research Ethics approval (WREM) # 119219.

Corresponding Author:
Shawn Whitehead, PhD
Department of Anatomy and Cell Biology
454 Medical Sciences Building
The University of Western Ontario
London, Ontario
N6A 3K7
519 661-2111 x80440
shawn.whitehead@schulich.uwo.ca

Running Title: Evidence of lipid peroxidation in ALSP

Abstract

Adult-onset leukoencephalopathy with axonal spheroids and pigmented glia (ALSP) is a rare but underdiagnosed early-onset white matter disease with symptoms including behavioural changes, motor and cognitive decline, seizures and progression to unresponsive wakefulness syndrome and death within eight years. Genetic mutations in *CSF1R* have been identified in many but not all cases and little is known about the mechanisms behind pathologic progression. Herein, we use a novel multi-modal workflow co-registering magnetic resonance imaging (MRI), histology and lipidomic profiling with matrix-assisted laser desorption ionization mass spectrometry imaging (MALDI-MSI) on post-mortem human tissue from donors with *CSF1R* mutation positive ALSP (n = 4), *CSF1R* mutation negative ALSP (n = 3) and no significant neuropathology (n = 4). This multi-modal workflow revealed convergent evidence of vascular dysregulation, iron dyshomeostasis, microglial dysfunction, and abnormal lipid peroxidation cascades. These results support a mechanistic hypothesis linking BBB insufficiency, iron accumulation, and dysregulated microglial response to lipid peroxidation in ALSP pathogenesis.

Keywords: ALSP, microglia, OxPC, lipids, white matter hyperintensity, iron

Introduction

Adult-onset leukoencephalopathy with axonal spheroids and pigmented glia (ALSP) is a progressive, early onset, neurodegenerative disease with an average life expectancy of eight years from symptom onset. ALSP is associated with hallmark white matter lesions and a vast range of devastating symptoms including personality changes, seizures, dementia and decline to unresponsive wakefulness syndrome. The colony-stimulating factor 1 receptor (CSF1R) gene is enriched in microglia in the brain and heterozygous mutation of this gene is one of the greatest risk factors for the development of ALSP[1,2]. However, not all cases of ALSP are positive for a CSF1R mutation and not every individual with a CSF1R mutation will be symptomatic[3]. Incomplete penetrance occurs even within families indicating that a secondary stressor in addition to the CSF1R mutation may be required to precipitate symptoms[3]. Collectively, the pathological mechanism underlying ALSP progression is poorly understood.

In ALSP, white matter changes can be observed as early as six years prior to symptom onset[4]. Magnetic resonance imaging (MRI) of ALSP typically reveals vast T_2 fluid-attenuated inversion recovery (FLAIR) white matter hyperintensities (WMH) with sparing of the subcortical u-fibres (SubU)[5]. Other hallmarks include: global and focal brain atrophy, thinning of the cortex and corpus callosum, dilation of the ventricles and calcifications seen on computed tomography[5]. Pathologically, ALSP is characterized by axonal loss, neuroaxonal spheroids and widespread white matter degeneration with pigmented macrophages and lesions of both microgliosis/macrophage infiltration and microglial depletion[5]. Ultrastructural characterization has further revealed lipid laden macrophages/microglia containing myelin debris within white matter lesions[6]. As is the case with many other neurological conditions, microglial dysfunction and altered lipid metabolism are

emerging as central players in ALSP pathogenesis. A recent transcriptomic and protein-level analyses of microglia in ALSP revealed patterns of increased activation, altered lipid metabolism and oxidative stress in persisting microglia[7]. This study also further validated the finding of lipid laden microglia and paralleled the microglia in ALSP with lipid-droplet accumulating microglia (LDAM) previously reported in Alzheimer's disease (AD) with APOE4/APOE4 or APOE3/APOE3 alleles[8,9]. Moreover, the only successful interventions for ALSP have been those that serve to replace microglia through invasive measures including hematopoietic stem cell transplantation (HSCT)[10] and more recently bone marrow cell (BMC) infusion[11]. However, these therapeutics are invasive and not without risk. BMC infusion has only recently emerged in a research capacity, and while some patients receiving HSCT demonstrate significant clinical benefit others experience worsening symptoms and even death[10]. Ultimately, understanding the mechanism of microglial dysfunction and the cause of incomplete penetrance in ALSP may prove critical for the development of future therapeutics.

Despite the connection between dysregulated lipid metabolism, microglial dysfunction and increased oxidative stress, the molecular identity of lipids accumulating in ALSP lesions has yet to be elucidated. Previous work has demonstrated evidence of blood brain barrier (BBB) breakdown and iron dyshomeostasis in ALSP both pre and post-mortem[12]. Ferroptosis is an iron mediated form of regulated cell death characterized by the buildup of reactive oxygen species (ROS) and dysregulated lipid metabolism resulting in an unchecked cascade of lipid peroxidation irreversibly damaging cellular membranes. White matter is highly susceptible to lipid peroxidation cascades due to its large percentage of myelinated axons[13,14] and ferroptosis in microglia has been linked to aging, neurodegenerative disease and specifically white matter pathology in both AD and

vascular dementia[15]. Dysregulated lipid peroxidation cascades may be an unexplored mechanism of pathological progression in ALSP.

Phosphatidylcholines (PCs) are a class of lipid that are enriched within biological membranes and vulnerable to lipid peroxidation due to their unsaturated fatty acid residue. Oxidized PCs (OxPCs) are the product of PC peroxidation and are the most characterized lipid peroxide[16]. Microglia are known to co-localize with OxPCs in a range of neurodegenerative diseases and *in vitro* have been found to play a critical role in protecting neurons through OxPC scavenging[17]. Furthermore, OxPCs are well established to exert neurotoxic effects both *in vitro* and *in vivo*[17] and through both enzymatic and hydrolysis reactions, OxPCs can be converted to Lyso-PC's (LPC) which are known demyelinating agents when overexpressed in the central nervous system (CNS)[18]. We hypothesize that microglia in ALSP exhibit a dysregulated response to lipid peroxidation such that BBB insufficiency and iron dyshomeostasis drive an unchecked lipid peroxidation cascade in the ALSP brain. We employ a novel multi-modal framework co-registering MRI, histology and lipidomic profiling with matrix-assisted laser desorption ionization mass spectrometry imaging (MALDI-MSI) to interrogate this hypothesis in post-mortem human tissue from donors with *CSF1R* mutation positive ALSP (n = 4), *CSF1R* mutation negative ALSP (n = 3) and no significant neuropathology (n = 4). Our results present evidence that vascular dysregulation, iron dyshomeostasis, microglial dysfunction and abnormal lipid peroxidation cascades serve as novel potential mechanisms for ALSP pathogenesis.

Methods

Tissue Samples and research ethics

ALSP donor brain tissues were obtained from the Dale E. Creighton London Brain Bank and the Pathology Department at London Health Sciences Centre (London, Ontario, Canada). Brain tissues from donors without ALSP nor other significant neuropathologies were provided by the BioRepository and Integrated Neuropathology (BRaIN) laboratory and the Precision Neuropathology Core at the University of Washington (UW) in Seattle, Washington, USA. **Table 1** summarizes the neuropathological features of the tissue donors utilized in this study. The mean age of ALSP donors with CSF1R mutation was 54 years. The mean age of ALSP donors with no known mutation was 60 years. The mean age of control donors no significant pathological diagnosis was 53 years. All research was conducted under research ethics board approval under Western Research Ethics approval (WREM) # 119219.

Tissue blocking

All tissue blocking for the ALSP samples was performed by the neuropathology teams at the Dale E. Creighton London Brain Bank and the Pathology Department at London Health Sciences Centre (London, Ontario, Canada). All tissue blocking for the control samples was performed by the teams at the BioRepository and Integrated Neuropathology (BRaIN) laboratory and the Precision Neuropathology Core at the UW (Seattle, Washington, USA). Following blocking tissue was placed in standard histological cassettes and stored in 10% formalin.

Magnetic resonance imaging

MRI scans were conducted at Western's Centre for Functional and Metabolic Mapping with a 7T Siemens Scanner according to a previously described protocol[19]. In summary, coronal tissue blocks were maintained in their histological cassettes but transferred to phosphate-buffered saline

(PBS) overnight. The next day they were then submerged and imaged in Galden HT-270 perfluorinated fluid in a custom-composite cylinder screw-lock container. A 3D T2-weighted FLAIR dataset was obtained using an inversion-prepared turbo spin-echo SPACE sequence (SPCIR) sequence (TR = 9000 ms, TE = 269 ms, TI = 2600 ms, ETL = 184, flip angle = 120°, matrix = 240×180×96, 0.4 mm isotropic resolution, GRAPPA R=2). A 3D T1-weighted dataset was acquired using an inversion-prepared spoiled gradient-echo MP2RAGE sequence (TR = 6000 ms, TE = 2.99 ms, matrix = 240×168×128, 0.4 mm isotropic resolution, GRAPPA R=2, partial Fourier = 0.75), with images reconstructed as bias-field–corrected UNI volumes.

Tissue Sectioning

Following MRI scans tissue blocks were hemisected coronally. Half the tissue was then paraffin embedded for histological assessment and the other half was flash frozen on dry ice for cryosectioning and MALDI-MSI. All paraffin embedding and sectioning of paraffin embedded tissue was done by the Molecular Pathology Core Facility at Western University (London, Ontario, Canada). Paraffin tissue was sectioned to 8 µm for histological assessment. All cryosectioning was done by N.O. using a cryostat (Thermo-Fisher Scientific CryoStar NX50, Toronto, Canada). The tissue was first secured to a cryostat chuck by freezing the base of the tissue to the chuck with deionized H_2O (dH_2O) over dry ice. Once secured, the tissue was acclimated in the cryostat at -21 °C for 15 minutes. The tissue was then sectioned to 10 µm using and thaw mounted onto indium tin oxide (ITO) coated slides for MALDI-MSI or onto Fisherbrand™ Superfrost™ Plus microscope slides for Oil-Red-O staining. For MALDI-MSI comparison of ALSP and control tissue, sections were thaw mounted onto the same ITO coated slide. **Figure 1** outlines the general workflow utilized.

Matrix Application for MALDI-MSI

Prior to matrix deposition slides were stored at -80 °C. Directly before sublimation they were dried for 5-10 minutes in room air and then placed into a vacuum desiccator for 15 minutes. 2,5-dihydroxybenzoic acid (DHB) matrix was applied to slides via sublimation as previously described[20]. To summarize, 300 mg of DHB matrix was measured and deposited evenly onto the bottom surface of the sublimation apparatus. The slides were then fixed directly above the matrix with the tissue sections facing down towards the matrix. The apparatus was then secured in place over a sand bath stabilized to 120 °C via hotplate. Under vacuum pressure the matrix was allowed to sublimate over the tissue for sixteen minutes. The slides were then placed in a -20 °C freezer overnight to allow for recrystallization. They were then desiccated for 15 minutes prior to being run then next day.

MALDI-MSI

MALDI-MSI data collection was in keeping with previously published work on formalin fixed post-mortem human brain tissue[17,21,22]. MALDI-MSI data was obtained with a Sciex 5800 TOF/TOF system, MALDI TOF/TOF (Sciex, Framingham, MA, USA) with a 349 nm Nd:YLF OptiBeam On-Axis laser with a pulse rate of 400 Hz. Prior to data collection the instrument was calibrated to a mass tolerance of 50 ppm based on a minimum of three peaks using Bruker Peptide Standards spotted adjacent to the tissue sections. All scans were conducted in reflectron positive mode and utilized a mass range of m/z 400−1000. All scans in this study employed a laser step

distance of 70 μm and were run with the same settings including laser intensity, shots per spectrum and detector voltage.

MALDI-MSI SCiLSLab Analysis

In order to convert MALD-MSI files into a format compatible with Bruker SCiLSLab Software, files were converted to imzML utilizing an R based code written by Dr. Mohammed Sarikahya[23]. MALDI-MSI analysis was initially conducted with Bruker SCiLSLab MVS Software (Version 2026a Premium 3D). In SCiLSLab MVS Software top-hat baseline subtraction and total ion count normalization was employed and the interval window was adjusted to 0.25 Da. Automatic spatial segmentation was utilized to aid in region of interest (ROI) selection (detailed in results). All ROIs used were manually selected. All principal component analysis (PCA), receiver operating characteristic (ROC) curves, and heatmap images were generated with SCiLSLab MVS Software. PCA analysis assessing different regions from one tissue section was conducted with five components, unit variance scaling, weak denoising and TIC normalization. PCA analysis pooling multiple tissue sections was conducted with eight components, pareto scaling, weak denoising and TIC normalization. ROC area under curve (AUC) threshold was automatically set to 0.75 and 0.25 but was increased to 0.65 and 0.35 respectively when the results produced less than 20 peak intervals and heatmaps that visually differentiated ROIs excluding isotopic peaks. All MALDI-MSI heatmap images representing lipids were obtained with weak denoising and hotspot removal. All MALDI-MSI heatmap images depicting calcium were obtained with no denoising and no hot spot removal to avoid signal suppression from more prominent lipid peaks. Peak area data from each ROI was exported and converted to CSV format for further multivariate analysis in

MetaboAnalyst 6.0 Software. Further details on multivariate analysis can be found within the designated methods subsection.

Identification of Peaks

Additional samples were prepped in the same manner as those for MALDI-MSI but were then subjected to tandem mass spectrometry (MSMS) in the Sciex 5800 TOF/TOF system, MALDI TOF/TOF (Sciex, Framingham, MA, USA). Reflectron positive mode was used to generate positive MSMS from parent peaks in the m/z 400–1000 range. TOF/TOF Series Explorer (Sciex) and Data Explorer (Sciex) software were utilized for data acquisition and data processing respectively. The top 40 features (top 20 elevated in ALSP WMH and top 20 elevated in control NAWM) were selected for tandem mass spectrometry analysis (MSMS). All other features were compared to pre-determined m/z values and lipid species in the literature and run through Lipids Maps® Structure Database (LMSD) and the Oxidized Phospholipid Database[24]. The most common positive mode ions were included in the search, including: $[M+H]^+$, $[M+K]^+$, $[M+Na]^+$. Mass tolerance was manually adjusted to 0.25 m/z in keeping with the interval width with SCiLSLab MVS Software and both PC and SM species were included in the search since this protocol is optimized for their detection.

MetaboAnalyst Multivariate Analysis

Additional multivariate analysis assessing the overall MALDI-MSI profiles was performed using MetaboAnalyst 6.0 Software without blinding[25]. No peaks were summed prior to analysis. The 30% of features with the lowest relative standard deviation for all samples were deemed to have near constant values between groups and were filtered out prior to analysis. The dataset was then

auto-scaled with no other filtering, normalization, transformation, or scaling methods employed. Sparse partial least squares discriminant analysis (sPLS-DA) analysis (8 components, 10 variables per component) was utilized to assess discrimination between groups. Model performance and reliable group discrimination was assessed using leave-one-out cross validation (LOOCV) and was deemed to have acceptable performance when a classification error rate of 25% or less was achieved.

Immunohistochemistry and Immunofluorescence

All immunohistochemistry (IHC) and histological staining with the exception of Oil-Red-O was completed by the Department of Pathology and Laboratory Medicine, University Hospital (London, Ontario, Canada). All immunofluorescence (IF) was completed by the Molecular Pathology Core Facility at Western University (London, Ontario, Canada).

Microscope images were acquired utilizing upright brightfield or fluorescent microscopy (Nikon Eclipse Ni-E, Nikon DS Fi2 colour camera, Nikon Qi2 fluorescent camera, NIS Elements Imaging; Mississauga, Ontario, Canada). All IF images panels comparing control to affected white matter in ALSP tissue were acquired and displayed with the same settings. An Aperio Whole-Slide Scanner was used to scan all slides used in this study (with the exception of IF slides), by Pathology Core Facilities at Western University. All histological evidence was reviewed with an accredited neuropathologist.

Results

Following the workflow outlined in **Figure 1**, FLAIR-MRI was used to confirm WMH in ALSP tissue blocks. The control blocks were confirmed to lack WMH while all ALSP blocks used in this

study possessed FLAIR-MRI defined WMH. Out of all of the tissue blocks utilized in this study, three from *CSF1R* mutation positive ALSP donors were identified by FLAIR-MRI to have regions of both WMH and NAWM within the same tissue block (**Figure 2A-C**). We validated the FLAIR-MRI regions of white matter damage with H&E and luxol fast blue (H&E/LFB) staining of sections from all tissue blocks utilized in this study. **Figure 2D-F** depicts the H&E/LFB staining of the three blocks containing both NAWM and WMH, demonstrating myelin pallor and tissue rarefaction in WMH regions compared to preserved myelin staining and normal architecture in NAWM.

Having confirmed distinct pathological regions by both MRI and histology, we next sought to determine whether MALDI-MSI lipidomic profiling could independently distinguish these regions based on their molecular signatures. Automatic segmentation with Bruker SCiLSLab software was applied to the positive mode MALDI-MSI scan of each tissue section independently (**Figure 2G-I**). This unsupervised spatial segmentation algorithm groups pixels with similar mass spectral profiles, enabling unbiased identification of molecularly distinct regions without prior knowledge of tissue anatomy or pathology. Automatic segmentation successfully visualized grey matter (GM), NAWM, WMH and subcortical U-fibers (SubU) within each of the sections, demonstrating that the lipidomic landscape alone could distinguish pathologically and anatomically distinct regions. The results of the FLAIR-MRI, H&E/LFB staining and the automatic segmentation were then used to inform the manual selection of regions of interest within these tissue sections (**Figure 2J-L**) to ensure accurate regional delineation for downstream quantitative analysis. Five component Principal component analysis (PCA) with unit variance scaling, TIC normalization and weak denoising of the MALDI-MSI data revealed distinct separation of ROIs for GM, WMH,

NAWM and SubU fibers in each individual donor (**Figure 2M-O**), with clear clustering and minimal overlap between groups. This further demonstrates that MALDI-MSI-derived lipidomic profiles can differentiate both neuroanatomical regions and pathologically affected white matter within the same tissue section, validating its use for spatially-resolved molecular profiling in ALSP. ROIs for all other tissue sections from remaining ALSP donors and controls were selected using the same integrative approach based on FLAIR-MRI, H&E/LFB and automatic segmentation of MALDI-MSI data. However, these sections exhibited only a single white matter state (either WMH in ALSP or NAWM in controls) and therefore could not be used for within-sample comparisons of WMH and NAWM.

We first sought to characterize lipid changes occurring in ALSP white matter lesions relative to mean age (within 1 year) and sex-matched controls without significant neuropathology. WMH identified with FLAIR-MRI in brain tissue from ALSP donors with confirmed CSF1R mutation were compared to NAWM within the same lobe of the brain from controls using MALDI-MSI. Each slide analyzed possessed one ALSP tissue section and the respective matched control tissue section. All settings for matrix application and MALDI-MSI data acquisition were preserved throughout (see methods for further details). ROC (0.75 and 0.25 discrimination threshold) on SCiLSLab software was used to identify the most discriminating lipids between NAWM from control tissue sections (n = 4) relative to WMH in CSF1R mutation positive ALSP tissue sections (n = 4). The complete list of most discriminating lipid species can be found in **Table 2.** Among the lipid species elevated in ALSP white matter lesions, we identified oxidized phosphatidylcholines including PAzPC and PONPC (**Figure 3A,B**), oxidized PCs with various chain lengths (PC 25:3;O2, PC 27:0;O, PC 32:5;O; **Figure 3C,D,G**), sphingomyelins (SM

34:1;O2, SM 34:2;O2, SM 36:2;O2, SM 36:1;O2; **Figure 3E,F,H,I**), and non-oxidized PCs (PC 33:3; **Figure 3J**). In contrast, lipid species elevated in control white matter included short-chain PCs (PC 12:4, PC 14:0; **Figure 3K,L**), lysophosphatidylcholines (LPC 17:0, LPC 16:0, LPC 22:6, LPC 24:0; **Figure 3M,O,Q,R**), ether-linked PCs (PC O-18:0, PC O-27:2; **Figure 3N,S**), and long-chain polyunsaturated PCs (PC 36:7; **Figure 3T**), in addition to one unidentified PC or SM species confirmed by tandem mass spectrometry (**Figure 3P**).

Having identified individual discriminating lipid species, we next evaluated whether the complete MALDI-MSI-derived lipidomic profile could classify tissue samples when considering all detected lipids simultaneously. We compared CSF1R mutation positive ALSP WMH regions (n=4) to CSF1R mutation positive ALSP grey matter (GM, n=4) and NAWM from control donors (n=4). **Figure 3U** depicts sample mass spectra from CSF1R mutation positive ALSP WMH, CSF1R mutation positive ALSP gray matter, and control NAWM. Sparse Partial Least Squares Discriminant Analysis (sPLS-DA) was selected for multivariate analysis as this supervised technique enabled dimensionality reduction while enhancing group separation, allowing for the visualization of lipid-based discrimination across the predefined classes of interest. Peak area data from each ROI was exported from SCiLsLab and uploaded to MetaboAnalyst software where the relative standard deviation (RSD = SD/mean) was used to filter out 30% of features with near constant values between groups prior to analysis and the dataset was auto-scaled. The synchronized 3D plot from sPLS-DA (8 components, 10 variables per component), with peak areas pertaining to ALSP CSF1R mutation positive WMH ($CSF1R^+$ WMH, n=4), ALSP $CSF1R^+$ gray matter ($CSF1R^+$ GM, n=4) and control NAWM (Control NAWM, n=4) ROIs revealed clear discrimination (**Figure 3V**). Model performance was assessed using Leave-One-Out Cross-

Validation (LOOCV) and achieved a classification error rate of 25%, supporting the reliability of lipid-based discrimination across these brain regions and WM disease states.

To determine whether ALSP cases without identified CSF1R mutations exhibit similar lipidomic changes, we explored the spatial clustering of WMH from clinically diagnosed ALSP donors with no known mutations (n=3) within this discriminant model. The sPLS-DA was repeated with the inclusion of two new datasets: no mutation ALSP WMH (NM WMH, n=3) and NM ALSP GM (NM GM, n=3). This analysis allowed for visualization of the relationship between this cohort with no known mutation and the existing brain regions and WM disease states (ALSP vs control) in the reduced component space. Since the NM cohort only had an n = 3 from one affected family, this discriminant analysis model was only used to visually inspect the clustering relationship. Visually, the NM GM clustered with the GM from the ALSP CSF1R mutation positive cohort, while the NM WMH clustered with the WMH from the ALSP CSF1R mutation positive cohort (**Figure 3W**). Based on the observed clustering, the sPLS-DA was repeated combing CSF1R mutation positive and NM ALSP cohorts. The sPLS-DA model was successfully (LOOCV = 22.2%) able to discriminate ALSP WMH (n = 7) from ALSP GM (n=7) and control NAWM group (n=4) with the MALDI-MSI derived lipid profiles (**Figure 3X**).

To identify lipid changes specifically associated with white matter pathology while controlling for inter-individual variability, we performed within-sample comparisons of WMH and NAWM regions in the three CSF1R mutation positive ALSP donors that possessed both tissue states (Figure 2). **Figure 4A** showcases just the WMH and NAWM ROIs with WMH outlined in red, and the NAWM outlined in blue. With the MALDI-MSI lipidomic data derived from these regions we first conducted an eight component PCA, grouping the WMH and NAWM regions from all

three specimens with pareto scaling, weak denoising and TIC normalization, to visualize spectral differences between ROIs. **Figure 4B** showcases the scores plot of this analysis, where each dot marker represents a mass spectrum acquired across one of the three samples and those from WMH regions are coloured red, while those from NAWM regions are coloured blue. Receiver operating characteristic (ROC) analysis (0.65 and 0.35 distinction threshold) was then used to ascertain lipid species capable of differentiating the WMH regions from the NAWM regions, combining all three tissue samples. **Table 3** lists all lipid species found to discriminate these two regions. Among the sphingomyelins elevated in WMH regions were SM 32:3;O2 (AUC = 0.715; **Figure 4C,D**) and SM 34:1;O2 (AUC = 0.738; **Figure 4E,F**), both of which showed spatial distributions matching FLAIR-MRI defined WMH. In contrast, longer-chain non-oxidized phosphatidylcholines were elevated in NAWM, including PC 39:4 (AUC = 0.185; **Figure 4G,H**) and PC 42:7 (AUC = 0.195; **Figure 4I,J**), suggesting preserved normal membrane lipid composition in these regions.

Since MALDI-MSI is by nature semi-quantitative due to a multitude of factors both biological and technical influencing molecular ionization, we then sought to analyze each tissue section in isolation to avoid overlooking lipid species whose signal may be supressed by more abundant lipid species in grouped analysis as in **Figure 4**. ROC analysis (0.75 and 0.25 discrimination threshold) comparing WMH and NAWM from Donor 1, Donor 2 and Donor 3 was conducted independently. **Table 4** showcases the comprehensive list of discriminating lipid species based on individual ROC analysis of WMH and NAWM for the tissue sections from each of these respective donors. Among the lipid species found to be significantly upregulated in WMH in Donor 1 (**Figure 5A**), LPC 16:0 (m/z 496.26 +/- 0.25 Da) (**Figure 5B**), LPC 15:1 (m/z 518.25 +/- 0.24 Da) (**Figure 5C**)**,** PC 30:3;O2 (732.43 +/- 0.04 Da) (**Figure 5D**), SM 36:2;O2 (m/z 751.45 +/-0.25 Da) (**Figure 5E**), PC

(18:0/KODA) (754.45 +/- 0.25 Da) (**Figure 5F**), and PC 34:3 (756.43 +/- 0.17 Da) (**Figure 5G**), and possessed the clearest MALDI-MSI heatmaps relative to the WMH identified with FLAIR-MRI. Relative to the FLAIR-MRI identified WMH for Donor 2 (**Figure 5H**), SM 32:2;O2 (673. 55 +/- 0.25 Da) (**Figure 5I**), SM 34:1;O2 (725.43 +/- 0.25 Da) (**Figure 5J**), PC 28:2;O2 (728.40 +/- 0.21 Da) (**Figure 5K**), SM 35:1;O2 (739. 50 +/- 0.25 Da) (**Figure 5L**), SM 38:3;O2 (m/z 755.45 +/- 0.25 Da) (**Figure 5M**), and PC 34:3 (m/z 756.43 +/- 0.25 Da) (**Figure 5N**) were among the upregulated lipids with the clearest MALDI-MSI heatmaps. For Donor 3, relative to the FLAIR-MRI identified WMH (**Figure 5O**), LPC 16:0 (m/z 496.26 +/- 0.25) (**Figure 5P**), LPC 15:1 (m/z 518.25 +/- 0.24 Da) (**Figure 5Q**), SM 30:0;O2 (m/z 687.45 +/- 0.25 Da) (**Figure 5R**), SM 36:1;O2 (753.45 +/- 0.25 Da) (**Figure 5S**), PC 34:3 (756.43 +/- 0.17 Da) (**Figure 5T**), and PC 42:5 (m/z 864.66 +/- 0.25 Da) (**Figure 5U**) were among the clearest MALDI-MSI heatmap images.

Following the MALDI-MSI analysis we interrogated the histological correlates of the lipidomic changes identified in the ALSP tissue using the tissue blocks showcased in **Figure 1** with both NAWM and WMH ROIs. Oil-Red-O staining was used to assess neutral lipid accumulation with ALSP samples. Oil-Red-O staining revealed lipid laden ameboid cells in WMH in CSF1R mutation positive ALSP (**Figure 6A**). We then utilized Perls' Prussian Blue staining to assess iron accumulation which revealed punctate positivity predominantly within WMH regions (**Figure 6B**). On closer evaluation, some ameboid cells within WMH regions in CSF1R mutation positive ALSP stained positive for iron with Perls' Prussian Blue, while others took on a brown colouration likely reflecting lipofuscin (**Figure 6C**). We then assessed the accumulation of OxPCs in ALSP samples using the antibody E06 which specifically binds OxPCs. Spatially, E06 positivity was

observed to be elevated in regions of FLAIR-MRI defined WMH (**Figure 6D**). In contrast to MALDI-MSI, E06-based assessment of OxPCs enabled localization analysis at cellular resolution. To investigate the spatial relationship between microglia and OxPCs in ALSP, Iba-1 and E06 IF was employed. Unaffected white matter from ALSP donors (obtained from the cerebellum) demonstrated minimal to no E06 positivity and ramified microglia (**Figure 6F**), while OxPCs were found to co-localize with ameboid microglia in WMH (**Figure 6G**). Of the control samples utilized in this study overall IF signal was significantly lower in all but one block and therefore these were excluded from IF comparison. We then assessed ferritin light chain (FLC) and Iba-1 colocalization. Unaffected white matter from ALSP donors (cerebellum) again revealed ramified Iba-1 with minimal to no FLC positivity (**Figure 6H**), while WMH regions showed ameboid Iba-1 IF colocalizing with FLC positive signal (**Figure 6I**).

Based on the observations made with IF and the observed iron accumulation, we further interrogated glial morphology and vascular architecture with classical IHC for enhanced clarity and detail. All findings in **Figure 7** are derived from n=3 with the CSF1R mutation positive ALSP blocks being the three with both NAWM and WMH based on FLAIR-MRI (**Figure 2**). Non-ALSP control tissue blocks and unaffected cerebellar blocks from ALSP donors displayed ramified microglia with Iba-1 IHC, while affected ALSP tissue blocks displayed a range of microglial morphology including ameboid, hypertrophic and dystrophic microglia (**Figure 7A**). We then further assessed both microglia (Iba-1) and astrocyte/ glial fibrillary acidic protein (GFAP) morphology in NAWM relative to WMH within the ALSP brain. **Figure 7B and C** depict representative ROIs from Donor 2 both on a FLAIR-MRI image and H&E and luxol fast blue stained section respectively. In NAWM, Iba-1 IHC showed dystrophic appearing microglia with

beaded appearing ramifications (**Figure 7D**), some human leukocyte antigen -DR isotope (HLADR) positivity (**Figure 7E**) and, densely packed glial fibrillary acidic protein (GFAP) positive astrocytic processes with small cell bodies (**Figure 7F**). The first ROI was selected directly in the middle of the WMH (WMH ROI 1) and subsequent Iba-1 IHC revealed predominantly ameboid microglia (**Figure 7G**) as well as, prominent HLADR positivity (**Figure 7H**) and gemistocytic astrocytes with enlarged cell bodies and more diffuse GFAP positive processes (**Figure 7I**). The more punctate WMH ROI 2 was selected in the middle of more NAWM and revealed densely populated ameboid Iba-1 microglia localized within the WMH (**Figure 7J**), dense HLADR positivity (**Figure 7K**) and gemistocytic astrocytes (**Figure 7L**). We then turned to Movat's pentachrome staining to assess vasculature. First, we noted punctate crystalloid appearing deposits frequently observed around blood vessels (**Figure 7M**) Oil-Red-O staining for neutral lipid deposition similarly showed lipid accumulation in a similar punctate pattern, but it remained unclear if this was staining vasculature or vasculature adjacent structures (**Figure 7N**). We then re-assessed the cortical vasculature with LFB/H&E. LFB/H&E staining similarly demonstrated crystalloid deposition in keeping with calcium deposition, a known hallmark of ALSP pathology, frequently occurring around blood vessels (**Figure 7O**). MALDI-MSI further validated the finding of punctate calcium deposition within the cortex and around blood vessels territories established with Movat's pentachrome staining, through the detection of DHB calcium adducts at m/z 538.91, m/z 730.87 and m/z 922.82 (**Figure 7P**). We then assessed the vascular architecture within the white matter. Movat's pentachrome staining exhibited evidence of sclerotic vessels within WMH.

Discussion

The present study advances the field in two principal ways: first, by introducing a novel methodological framework co-registering MRI, histology and lipidomic profiling with MALDI-MSI; and second, by uncovering previously unrecognized pathological findings linking abnormal microglial histology with lipid dysregulation, and iron dyshomeostasis in the post-mortem ALSP brain. These findings may one day serve as potential therapeutic targets in ALSP. While previous studies have co-registered either MALDI-MSI and histology[17,21] or MALDI-MSI and FLAIR-MRI[22] this study is the first of its kind to integrate all three modalities, successfully showcasing the ability of MALDI-MSI lipidomic profiling to distinguish both distinct neuroanatomical regions as well as regions within the same neuroanatomical territory that are differentially affected by disease pathology. This macro- to microscopic approach allows for characterization of clinically relevant MRI defined lesions at the cellular level with histological assessment and at the molecular level with MALDI-MSI *in situ* molecular mapping.

MALDI-MSI lipidomic profiling successfully differentiated distinct regions within ALSP tissue with confirmed *CSF1R* mutation and ALSP from control samples. The utilization of automatic segmentation of MALDI-MSI data as part of the ROI selection process (**Figure 2G-I**) allowed for unbiased pattern recognition within the dataset. This process validated our hypothesis that WMH in ALSP would exhibit distinct lipid profiles compared to adjacent NAWM within the sample. Since automatic segmentation is optimized for within sample analysis, we then used multivariate statistical approaches to interrogate the ability of this dataset to separate control samples NAWM regions (n=4) from ALSP with *CSF1R* mutation WMH regions (n=4) and ALSP with no known mutation WMH regions (n=3). This approach successfully differentiated ALSP from controls (**Figure 3**); however, an important limitation to acknowledge in this study is

sample size, and familial relationship between donors given that ALSP is a rare disease. Due to this limitation ALSP with no known mutation WMH regions were viewed in the context of control vs ALSP with *CSF1R* mutation which allowed for the visualization of data separation and then were combined as one ALSP cohort. While future studies are needed to determine the relationship between *CSF1R* mutation driven ALSP and cases with no known mutation, our work demonstrates that these patient populations exhibit similar PC and SM lipidomic profiles, possibly pointing to a similar pathological mechanism.

A key finding of this study is the elevation of OxPCs within ALSP WMH compared to control white matter (**Figures 3**), as well as a complex accumulation of distinct OxPCs and LPCs within ALSP WMH compared to adjacent NAWM (**Figure 5**). This coupled with histological assessment demonstrating that OxPCs colocalize with microglia at the cellular level (**Figure 6D-G**), elucidates a complex interplay in which OxPCs are associated with white matter lesions in ALSP and regions of microgliosis. OxPCs are established neurotoxic mediators, and microglia are critical first responders in mitigating OxPC-mediated damage both *in vitro* and *in vivo*[17]. Given that *CSF1R* mutation and microglial dysregulation is central in ALSP pathophysiology, this represents a potential mechanism by which microglia fail in the ALSP brain. Our results are in keeping with recent work by Du and colleagues that identified the microglia that persist in ALSP exhibit an altered transcriptomic profile in which they lose homeostatic signatures and exhibit signs of proinflammatory activation, altered lipid metabolism and oxidative stress responses[7]. This study also demonstrated upregulation of ferroptosis based gene expression and protein level accumulation of FTL[7], further in keeping with our finding of iron accumulation and FTL upregulation in microglia in ALSP WMH (**Figure 6B,C,H,I**). Given that CSF1R is essential for

484 microglial survival, proliferation, and function, mutations in this receptor may impair the
485 microglial response to OxPCs, leading to their pathological accumulation. This represents a
486 potential mechanism by which CSF1R mutation precipitates white matter degeneration:
487 dysfunctional microglia fail to clear OxPCs, allowing unchecked lipid peroxidation cascades that
488 irreversibly damage cellular membranes. Lipid peroxidation is a critical driver of ferroptosis
489 mediated pathology and cell death. It is therefore possible that iron dyshomeostasis coupled with
490 CSF1R mutation, leads to ferroptosis pathway activation and subsequent lipid peroxidation. More
491 work is needed to explore the temporal relationship in ALSP as it remains unclear based on post-
492 mortem assessment alone if OxPC accumulation precedes iron accumulation or vice versa.
493
494 The source of iron accumulation in ALSP remains unclear, but our study provides observational
495 evidence implicating vascular dysfunction. We observed calcium accumulation around blood
496 vessels and within vascular territories, as well as sclerotic vessels within WMH (**Figure 7M-Q**).
497 Although a preliminary and post-mortem findings, this suggests compromised vascular integrity.
498 Previous studies have also identified evidence of vascular dysregulation and BBB insufficiency in
499 ALSP. Post-mortem evaluation from ALSP patients revealed widespread cerebral amyloid
500 angiopathy, severe arteriosclerosis in subcortical white matter and perivascular accumulation of
501 phosphorylated tau in addition to abnormal claudin-5 distribution around blood vessels, IgG
502 extravasation and fibrinogen all suggestive of BBB insufficiency[12]. Pre-mortem, in a patient with
503 recent symptom onset, dynamic contrast enhanced MRI revealed evidence of BBB disruption both
504 cortically and in deep white matter while susceptibility weighted imaging demonstrated evidence
505 of iron deposition distributed similarly to the BBB disruption[12]. Further evidence suggestive of
506 BBB disruption in ALSP is the sparing of subU fibres. Since subU fibres boast an independent

blood supply and slower myelin turnover than other white matter tracts, they have been proposed as a sign-post for white matter disease mechanisms; being spared in vascular disorders and many hereditary leukodystrophies affecting myelin metabolism, but targeted in demyelinating conditions such as multiple sclerosis and infectious diseases such as progressive multifocal leukoencephalopathy[26]. Additional work has also demonstrated perivascular localization of peripheral macrophages in the brain of ALSP patients[12] and donor chimerism in the cerebrospinal fluid of patients who received hematopoietic stem cell transplantation[27] which supports peripheral macrophage infiltration into the brain and provides additional evidence of a leaky BBB. Collectively, there is evidence of BBB insufficiency and vascular dysregulation in ALSP and it remains possible that the white matter devastation, adult-onset nature and incomplete penetrance of ALSP may in part be explained by insults to the BBB that are unique to individuals and accumulate throughout life.

Alternatively, it is possible that white matter devastation occurs first in ALSP as a demyelinating pathology and vascular dysregulation and iron accumulation follow. Oligodendrocytes are the most iron rich cell within the CNS[28], and microglia are critically implicated in their homeostasis[29]. Du and colleague's results showcased complex genetic changes in oligodendrocytes in ALSP parallelling both multiple sclerosis and AD oligodendrocyte signatures, such that there was an upregulation of $NRP2^{+}$ oligodendrocytes expressing stress-related and apoptotic signatures while myelinating oligodendrocytes were reduced[7]. They purposed astrocytes may compensate for lipid clearance in the absence of microglia or in the presence of dysregulated microglia leading to a maladaptive environment for oligodendrocytes and myelination[7]. Our observation of LPC accumulation in ALSP WMH is consistent with ongoing demyelination, as LPCs are known

demyelinating agents when overexpressed in the CNS[18]. The elevated oxidized sphingomyelins we observe may similarly reflect breakdown of myelin membranes, which are particularly enriched in sphingomyelin content. Regardless of the mechanism by which it occurs, iron dyshomeostasis is known to be a critical driver of oxidative stress and lipid peroxidation.

In addition to OxPCs other lipid profiles may help imply the pathological mechanisms driving ALSP. SM 34:1;O2 was among the lipids upregulated in ALSP WMH (**Figure 3E, Figure 4E, Figure 5J**) and has previously been proposed as a marker for stroke-damaged tissue[30]. Moreover, SM 34:1;O2 has previously been shown to exist predominantly within hypoxic regions of breast tumors in addition to some other lipids including LPC 16:0[31]. LPC 16:0 was also among the short-chain LPCs found to be upregulated in a cuprizone model of demyelination, but notably it remained elevated in the group that underwent subsequent remyelination post exposure[32]. Intriguingly, while our results found LPC 16:0 was among the lipids elevated in ALSP WMH compared to within sample NAWM (**Figure 5B,P**), it was upregulated in control NAWM relative to ALSP WMH (**Figure 3O**), suggesting that it may not be a pathology specific finding, but rather related to post-mortem tissue. Short-chain LPCs in addition to non-oxidized PCs were among the lipids most prevalent in the controls relative to the ALSP brains (**Figure 3**). A much more complex picture evolved through comparison of ALSP WMH to NAWM (**Figure 5, Table 4**) in which distinct OxPCs and LPCs were associated with both regions. It is important to note NAWM with ALSP brain tissue is an MRI designation, and that adjacent NAWM regions demonstrated largely abnormal histological findings, including dystrophic appearing microglia (**Figure 7D**) and HLA-DR positivity (**Figure 7E**). Distinct lipids within adjacent NAWM bordering WMH (**Table 4**) may prove critical to understanding lesion expansion mechanisms in ALSP. Another important

limitation with human tissue is that is post-mortem interval and tissue processing is often variable. We combat this through combining grouped analysis with individual within sample comparisons and through validation with IHC and IF approaches. Additionally, as MALDI-MSI technology evolves the ability to confirm lipid identity beyond MSMS and improved spatial resolution will allow for enhanced lipidomic characterization at the cellular level in different disease states.

This study integrates FLAIR-MRI, histological assessment, and MALDI-MSI in a multi-modal approach to characterizing white matter lesions in ALSP, providing both a methodological framework for future white matter disease studies and novel mechanistic insights. Our findings reveal that ALSP white matter lesions are characterized by accumulation of OxPCs and sphingomyelins colocalizing with iron-laden, dysfunctional microglia in the context of vascular pathology including sclerotic vessels and calcium deposition. These converging observations suggest that BBB breakdown permits iron extravasation, triggering ferroptosis and lipid peroxidation cascades that overwhelm dysfunctional CSF1R-mutant microglia. This work identifies potential therapeutic targets including ferroptosis inhibition and antioxidant therapy, offering a novel targetable mechanism for a disease currently limited to invasive hematopoietic stem cell transplantation with significant mortality risk. Collectively, our work presents vascular dysregulation, iron dyshomeostasis, microglial dysfunction, and abnormal lipid peroxidation cascades as convergent, interrelated mechanisms driving ALSP pathogenesis.

Data Availability

At the discretion of the authors data can be made available upon at request.

Acknowledgements

We would foremost like to thank the donors and their families for their contribution to science. Without them, this work would not be possible. We would also like to thank a number of individuals who showed interest in this work and helped make the data collection possible including Dr. Mohammed Sarikahya who wrote the code used for imzML conversion, Dr. Jacob Houpt who blocked additional samples, Dr. Chaochao Chen who assisted with MSMS acquisition and MALDI-MSI operations, Dr. Lin Zhao who offered expert microscopy insight, Dr. Lynn Wang who made the day to day operations possible, Dr. Austyn Roseborough who provided guidance on MRI analysis, Mu Han Liu who assisted with MRI tissue preparation, Caroline O'Neil who led the Molecular Pathology Core Facility team that worked on this project, and Isabella Boesgaard and Meaghan Frank who have been a part of driving future directions.

Competing Interests

The authors report no competing interests.

Funding

This project was supported by the Canadian Institutes for Health Research (CIHR) [202104PJT-461038] and the Natural Sciences and Engineering Research Council of Canada (NSERC) [RGPIN-2019-04742] to SNW. NO was supported by CIHR Canada Graduate Scholarships Doctoral Awards and by the Kappa Kappa Gamma (KKG) Foundation of Canada. The UW BioRepository and Integrated Neuropathology (BRaIN) Laboratory and Precision Neuropathology Core are supported by the National Institutes of Health (NIH) through the UW Alzheimer's

598 Disease Research Center (P30AG066509), the Adult Changes in Thought (ACT) study
599 (U19AG066567 and R01AG060942), the BRAIN Initiative Cell Atlas Network (UM1 MH130981
600 and UM1MH134812), the Seattle Alzheimer's Disease Brain Cell Atlas (U19AG060909), the
601 Allen Institute for Brain Science, and the Nancy and Buster Alvord Endowment.
602

References

1. Konno T, Yoshida K, Mizuno T, et al. Clinical and genetic characterization of adult-onset leukoencephalopathy with axonal spheroids and pigmented glia associated with CSF1R mutation. *Eur J Neurol*. 2017;24(1):37-45. doi:10.1111/ene.13125

2. Papapetropoulos S, Gelfand JM, Konno T, et al. Clinical presentation and diagnosis of adult-onset leukoencephalopathy with axonal spheroids and pigmented glia: a literature analysis of case studies. *Front Neurol*. 2024;15. https://www.frontiersin.org/journals/neurology/articles/10.3389/fneur.2024.1320663

3. Dulski J, Muthusamy K, Lund TC, Wszolek ZK. CSF1R-related disorder: State of the art, challenges, and proposition of a new terminology. *Parkinsonism Relat Disord*. Published online October 10, 2023:105894. doi:10.1016/j.parkreldis.2023.105894

4. Van Gerpen JA, Wider C, Broderick DF, Dickson DW, Brown LA, Wszolek ZK. Insights into the dynamics of hereditary diffuse leukoencephalopathy with axonal spheroids. *Neurology*. 2008;71(12):925. doi:10.1212/01.wnl.0000325916.30701.21

5. Papapetropoulos S, Pontius A, Finger E, et al. Adult-Onset Leukoencephalopathy With Axonal Spheroids and Pigmented Glia: Review of Clinical Manifestations as Foundations for Therapeutic Development. *Front Neurol*. 2022;12. https://www.frontiersin.org/journals/neurology/articles/10.3389/fneur.2021.788168

6. Lin WL, Wszolek ZK, Dickson DW. Hereditary diffuse leukoencephalopathy with spheroids: ultrastructural and immunoelectron microscopic studies.

7. Du S, Zhou Y, Li D, et al. Mutations in the human CSF1R gene impact microglia's maintenance of brain white matter integrity. *Nat Immunol*. 2025;26(7):1198-1211. doi:10.1038/s41590-025-02195-7

8. Marschallinger J, Iram T, Zardeneta M, et al. Lipid-droplet-accumulating microglia represent a dysfunctional and proinflammatory state in the aging brain. *Nat Neurosci*. 2020;23(2):194-208. doi:10.1038/s41593-019-0566-1

9. Haney MS, Pálovics R, Munson CN, et al. APOE4/4 is linked to damaging lipid droplets in Alzheimer's disease microglia. *Nature*. 2024;628(8006):154-161.

10. Dulski J, Heckman MG, White LJ, Żur-Wyrozumska K, Lund TC, Wszolek ZK. Hematopoietic Stem Cell Transplantation in CSF1R-Related Leukoencephalopathy: Retrospective Study on Predictors of Outcomes. *Pharmaceutics*. 2022;14(12). doi:10.3390/pharmaceutics14122778

11. Wu J, Wang Y, Li X, et al. Microglia replacement halts the progression of microgliopathy in mice and humans. *Science*. 389(6756):eadr1015. doi:10.1126/science.adr1015

12. Delaney C, Farrell M, Doherty CP, et al. Attenuated CSF-1R signalling drives cerebrovascular pathology. *EMBO Mol Med*. Published online 2020.

13. Salim S. Oxidative Stress and the Central Nervous System. *J Pharmacol Exp Ther*. 2017;360(1):201-205. doi:10.1124/jpet.116.237503

14. Gonzalo H, Brieva L, Tatzber F, et al. Lipidome analysis in multiple sclerosis reveals protein lipoxidative damage as a potential pathogenic mechanism. *J Neurochem*. 2012;123(4):622-634. doi:10.1111/j.1471-4159.2012.07934.x

15. Adeniyi PA, Gong X, MacGregor E, et al. Ferroptosis of Microglia in Aging Human White Matter Injury. *Ann Neurol*. 2023;94(6):1048-1066. doi:10.1002/ana.26770

16. Dong Y, Yong VW. Oxidized phospholipids as novel mediators of neurodegeneration. *Trends Neurosci*. 2022;45(6):419-429. doi:10.1016/j.tins.2022.03.002

17. Dong Y, D'Mello C, Pinsky W, et al. Oxidized phosphatidylcholines found in multiple sclerosis lesions mediate neurodegeneration and are neutralized by microglia. *Nat Neurosci*. 2021;24(4):489-503. doi:10.1038/s41593-021-00801-z

18. Plemel JR, Michaels NJ, Weishaupt N, et al. Mechanisms of lysophosphatidylcholine-induced demyelination: A primary lipid disrupting myelinopathy. *Glia*. 2018;66(2):327-347. doi:10.1002/glia.23245

19. Roseborough AD, Langdon KD, Hammond R, et al. Post-mortem 7 Tesla MRI detection of white matter hyperintensities: A multidisciplinary voxel-wise comparison of imaging and histological correlates. *NeuroImage Clin*. 2020;27:102340. doi:10.1016/j.nicl.2020.102340

20. Caughlin S, Park DH, Yeung KKC, Cechetto DF, Whitehead SN. Sublimation of DAN Matrix for the Detection and Visualization of Gangliosides in Rat Brain Tissue for MALDI Imaging Mass Spectrometry. *J Vis Exp*. 2017;(121):e55254. doi:10.3791/55254

21. Ollen-Bittle N, Pejhan S, Pasternak SH, Keene CD, Zhang Q, Whitehead SN. Co-registration of MALDI-MSI and histology demonstrates gangliosides co-localize with amyloid beta plaques in Alzheimer's disease. *Acta Neuropathol (Berl)*. 2024;147(1):105. doi:10.1007/s00401-024-02759-1

22. Pinsky W, Harris A, Roseborough AD, et al. Regional Lipid Expression Abnormalities Identified Using MALDI IMS Correspond to MRI-Defined White Matter Hyperintensities within Post-mortem Human Brain Tissues. *Anal Chem*. 2021;93(4):2652-2659. doi:10.1021/acs.analchem.0c05017

23. Sarikahya M. imzmlconvertor. GithHub. August 25, 2025. https://github.com/MHSarikahya/imzmlconvertor/releases/tag/0.1

24. LIPID MAPS® Structure Database (LMSD). LipidMaps. https://www.lipidmaps.org/resources/tools/bulk-structure-search/create?database=LMSD

25. Pang Z, Lu Y, Zhou G, et al. MetaboAnalyst 6.0: towards a unified platform for metabolomics data processing, analysis and interpretation. *Nucleic Acids Res*. 2024;52(W1):W398-W406. doi:10.1093/nar/gkae253

26. Riley KJ, O'Neill DP, Kralik SF. Subcortical U-Fibers: Signposts to the Diagnosis of White Matter Disease. *Neurographics*. 2018;8(4):234-243. doi:10.3174/ng.1700048

27. Tipton PW, Kenney-Jung D, Rush BK, et al. Treatment of -Related Leukoencephalopathy: Breaking New Ground. *Mov Disord*. 2021;36(12):2901-2909. doi:10.1002/mds.28734

28. Connor JR, Menzies SL. Relationship of iron to oligondendrocytes and myelination. *Glia*. 1996;17(2):83-93. doi:10.1002/(SICI)1098-1136(199606)17:2<83::AID-GLIA1>3.0.CO;2-7

29. McNamara NB, Munro DAD, Bestard-Cuche N, et al. Microglia regulate central nervous system myelin growth and integrity. *Nature*. 2023;613(7942):120-129. doi:10.1038/s41586-022-05534-y

30. Henderson F, Hart PJ, Pradillo JM, et al. Multi-modal imaging of long-term recovery post-stroke by positron emission tomography and matrix-assisted laser desorption/ionisation mass spectrometry. *Rapid Commun Mass Spectrom*. 2018;32(9):721-729. doi:10.1002/rcm.8090

31. Chughtai K, Jiang L, Greenwood TR, Glunde K, Heeren RMA. Mass spectrometry images acylcarnitines, phosphatidylcholines, and sphingomyelin in MDA-MB-231 breast tumor models [S]. *J Lipid Res*. 2013;54(2):333-344. doi:10.1194/jlr.M027961

32. Opielka M, Urbanowicz K, Konieczna-Wolska K, et al. Spatial lipidomics reveals demyelination and remyelination dynamics in the mouse brain. *J Lipid Res*. Published online September 23, 2025:100912. doi:10.1016/j.jlr.2025.100912

Figure 1. Workflow. Brains from donors with ALSP and CSF1R mutation, ALSP and no known mutation and controls with no significant pathological diagnosis were dissected into tissue blocks standard cassette sized and then subjected to 7T FLAIR-MRI. Following MRI the tissue blocks were then hemisected coronally with half being flash frozen and cryo-sectioned for MALDI-MSI and the other being paraffin embedded for histological assessment. Created with BioRender.com.

Figure 2. Multi-modal imaging reveals distinct lipidomic signatures in ALSP white matter lesions. Post-mortem tissue blocks from three CSF1R mutation-positive ALSP donors containing both white matter hyperintensities (WMH) and normal-appearing white matter (NAWM) were subjected to sequential analysis. A-C) 7T FLAIR-MRI identified regions of WMH (hyperintense signal) and NAWM. D-F) H&E/LFB staining confirmed myelin loss and tissue rarefaction in WMH regions with preserved architecture in NAWM. G-I) Unsupervised automatic segmentation of MALDI-MSI data independently identified molecularly distinct regions corresponding to grey matter (GM), NAWM, WMH, and subcortical U-fibers (SubU), demonstrating that lipidomic profiles distinguish both neuroanatomical and pathological states.

J-L) Manual region of interest (ROI) selection integrated findings from FLAIR-MRI, histology, and automatic segmentation. M-O) Principal component analysis (PCA) revealed distinct clustering of ROIs, confirming that MALDI-MSI can differentiate pathologically affected white matter from adjacent NAWM within the same tissue section. Each point represents a single mass spectrum. Scale bar = 5 mm.

Figure 3. Distinct lipid changes occur in ALSP white matter lesions relative to mean age and sex-matched controls. White matter hyperintensities (WMH) identified with FLAIR-MRI in brain tissue from ALSP donors with confirmed CSF1R mutation were compared to normal appearing white matter (NAWM) within the same lobe of the brain from mean age (within 1 year) and sex-matched controls using MALDI-MSI. Receiver operating characteristic (ROC) on SCiLSLab software was used to identify the most discriminating lipids (0.75 and 0.25 discrimination threshold). The complete list of most discriminating lipid species can be found in Table 2. Tentative identities of lipids elevated in ALSP white matter lesions included A) PAzPC, B) PONPC, C) PC 25:3;O2, D) PC 27:0;O, E) SM 34:1;O2, F) SM 34:2;O2, G) PC 32:5;O, H) SM 36:2;O2, I) SM 36:1;O2, J) PC 33:3. Tentative identity of lipids elevated in control white matter included K) PC 12:4, L) PC 14:0, M) LPC 17:0, N) PC O-18:0, O) LPC 16:0, P) and unknown PC or SM species confirmed with MSMS, Q) LPC 22:6, R) LPC 24:0, S) PC O-27:2, T) PC 36:7. U) Sample mass spectra from ALSP WMH, ALSP gray matter, and control NAWM. V) Synchronized 3D plot from sparse partial least squares discriminant analysis (sPLS-DA), (8 components, 10 variables per component), with peak areas pertaining to ALSP CSF1R mutation positive ($CSF1R^+$) WMH (n=4), ALSP $CSF1R^+$ gray matter (GM) (n=4) and control NAWM (n=4) ROIs revealed clear separation. W) sPLS-DA, (8 components, 10 variables per component), was then repeated adding in additional groups pertaining to No Mutation ALSP (NM) WMH (n=3), NM ALSP GM (n=3) ROIs. X) $CSF1R^+$ mutation positive and NM ALSP groups were then pooled (n=7) and compared to the control NAWM group (n=4) with sPLS-DA modeling revealing clear separation.

Figure 4. Distinct lipid changes occur in $CSF1R^+$ ALSP WMH compared to adjacent NAWM. A) White matter hyperintensities (WMH) outlined in red, were identified with FLAIR-MRI in brain tissue from ALSP donors with confirmed CSF1R mutation and were compared to adjacent normal appearing white matter (NAWM) outlined in blue, using MALDI-MSI. B) A scores plot of eight component principal component analysis (PCA) conducted on SciLs Lab software was used to visualize the distinction between WMH and NAWM. Each dot marker represents a spectrum. Receiver operating characteristic (ROC) analysis (0.65 and 0.35 distinction threshold) was then used to ascertain lipid species capable of differentiating the WMH regions from the NAWM regions in all three tissue samples. C)Heatmap image of SM 32:3;O2, D) which was found to be elevated in WMH regions based on ROC analysis (AUC = 0.715). E) Heatmap image of SM 34:1;O2, F) which was found to be elevated in WMH regions based on ROC analysis (AUC = 0.738). G) Heatmap image of PC 39:4, H) which was found to be elevated in NAWM regions based on ROC analysis (AUC = 0.185). I) Heatmap image of PC 42:7, HJ) which was found to be elevated in NAWM regions based on ROC analysis (AUC = 0.195). A complete list of lipids from this analysis can be found in Table 3.

Figure 5. Individual receiver operating characteristic (ROC) analysis of lipids upregulated in WMH of post-mortem tissue blocks from donors with CSF1R mutation positive ALSP. A) Donor 1 FLAIR-MRI with red box outlining the region sectioned and isolated for MALDI-MSI. B) Receiver operating characteristic (ROC) analysis (0.75 and 0.25 discrimination threshold) comparing WMH and NAWM for Donor 1 revealed distinct lipid species were upregulated within the WMH including: LPC 16:0 (m/z 496.26 +/- 0.25 Da) as well, C) LPC 15:1 (m/z 518.25 +/- 0.24 Da)**,** D), PC 30:3;O2 (754.45 +/- 0.25 Da), E) SM 36:2;O2 (m/z 751.45 +/-0.25 Da), F) PC (18:0/KODA) (754.45 +/- 0.25 Da), G) PC 34:3 (756.43 +/- 0.17 Da). H) Donor 2 FLAIR-MRI with red box outlining the region sectioned and isolated for MALDI-MSI. I) ROC analysis (0.75 and 0.25 discrimination threshold) comparing WMH and NAWM for Donor 2 revealed distinct lipid species were upregulated within the WMH including SM 32:2;O2 (673. 55 +/- 0.25 Da), J) SM 34:1;O2 (725.43 +/- 0.25 Da), K) PC 28:2;O2 (728.40 +/- 0.21 Da), L) SM 34:2;O2 (739. 50 +/- 0.25 Da), M) SM 38:3;O2 (m/z 755.45 +/- 0.25 Da), and N) PC 34:3 (m/z 756.43 +/- 0.25 Da). O) Donor 3 FLAIR-MRI with red box outlining the region sectioned and isolated for MALDI-MSI. P) ROC analysis (0.75 and 0.25 discrimination threshold) comparing WMH and NAWM for Donor 3 revealed distinct lipid species were upregulated within the WMH including: LPC 16:0 (m/z 496.26 +/- 0.25), Q) LPC 15:1 (m/z 518.25 +/- 0.24 Da)**,** R) SM 30:0;O2 (m/z 687.45 +/- 0.25 Da), S) SM 36:1;O2 (753.45 +/- 0.25 Da), T) PC 34:3 (756.43 +/- 0.17 Da), and U) PC 42:5 (m/z 864.66 +/- 0.25 Da).

Figure 6. Evidence of lipid laden microglia and pathological iron accumulation in ALSP. A) Oil-Red-O staining showed lipid laden ameboid cells in white matter hyperintensities in $CSF1R^+$ ALSP (n=3). B) Perls' Prussian Blue staining showed iron accumulation in WMH regions (n=3). C) Some ameboid cells within WMH regions in $CSF1R^+$ ALSP stained positive for iron with Perls' Prussian Blue, while others took on a brown colouration likely reflecting lipofuscin (n=3). D) FLAIR-MRI of a $CSF1R^+$ ALSP post-mortem sample with exert imaged for immunofluorescence (IF) outlined in red. E) IF panel showed increased Iba-1 and E06 accumulation in WMH region. F) Unaffected white matter (WM) taken from the cerebellum of donors revealed ramified Iba-1 IF with minimal to no E06 (OxPC) positivity. G) Affected WM showed ameboid Iba-1 IF colocalizing with E06 positive signal. H) Unaffected white matter (WM) taken from the cerebellum of donors revealed ramified Iba-1 IF with minimal to no ferritin light chain (FLC) positivity. I) Affected WM showed ameboid Iba-1 IF colocalizing with FLC positive signal.

Figure 7. Histological characterization of glia and vasculature in post-mortem ALSP brain tissue. A) Non-ALSP control tissue blocks and unaffected cerebellar blocks from ALSP donors displayed ramified microglia with Iba-1 immunohistochemistry (IHC), while affected ALSP tissue blocks exhibited a range of microglial morphology including ameboid, hypertrophic and dystrophic. B) FLAIR-MRI and C) Luxol fast blue/ hematoxylin and eosin (LFB/H&E) from an ALSP donor sample with imaged exerts outlined. D) In NAWM, Iba-1 IHC showed dystrophic appearing microglia with beaded appearing ramifications E) some human leukocyte antigen -DR isotope (HLADR) positivity and, F) densely packed glial fibrillary acidic protein (GFAP) positive processes and small cell bodies. G) WMH ROI 1 was selected in the middle of a WMH

and subsequent Iba-1 IHC showed predominantly ameboid microglia as well as, H) more prominent HLADR positivity and, I) gemistocytic astrocytes with enlarged cell bodies and more diffuse GFAP positive processes. J) the more punctate WMH ROI 2 was selected in the middle of more NAWM and revealed densely populated ameboid Iba-1 microglia as well as, K) HLADR positivity and, L) gemistocytic astrocytes. M) Within the cortex Movat's pentachrome staining revealed punctate crystalloid appearing deposits frequently observed around blood vessels while N) Oil-Red-O staining showed neutral lipid deposition in a similar punctate pattern. O) LFB/H&E staining similarly demonstrated crystalloid deposition in keeping with calcium deposition, a known hallmark of ALSP pathology, frequently occurring around blood vessels. P) MALDI-MSI further validated the finding of punctate calcium deposition within the cortex and around blood vessels territories established with Movat's pentachrome staining. Q) Movat's pentachrome staining further exhibited evidence of sclerotic vessels within WMH.

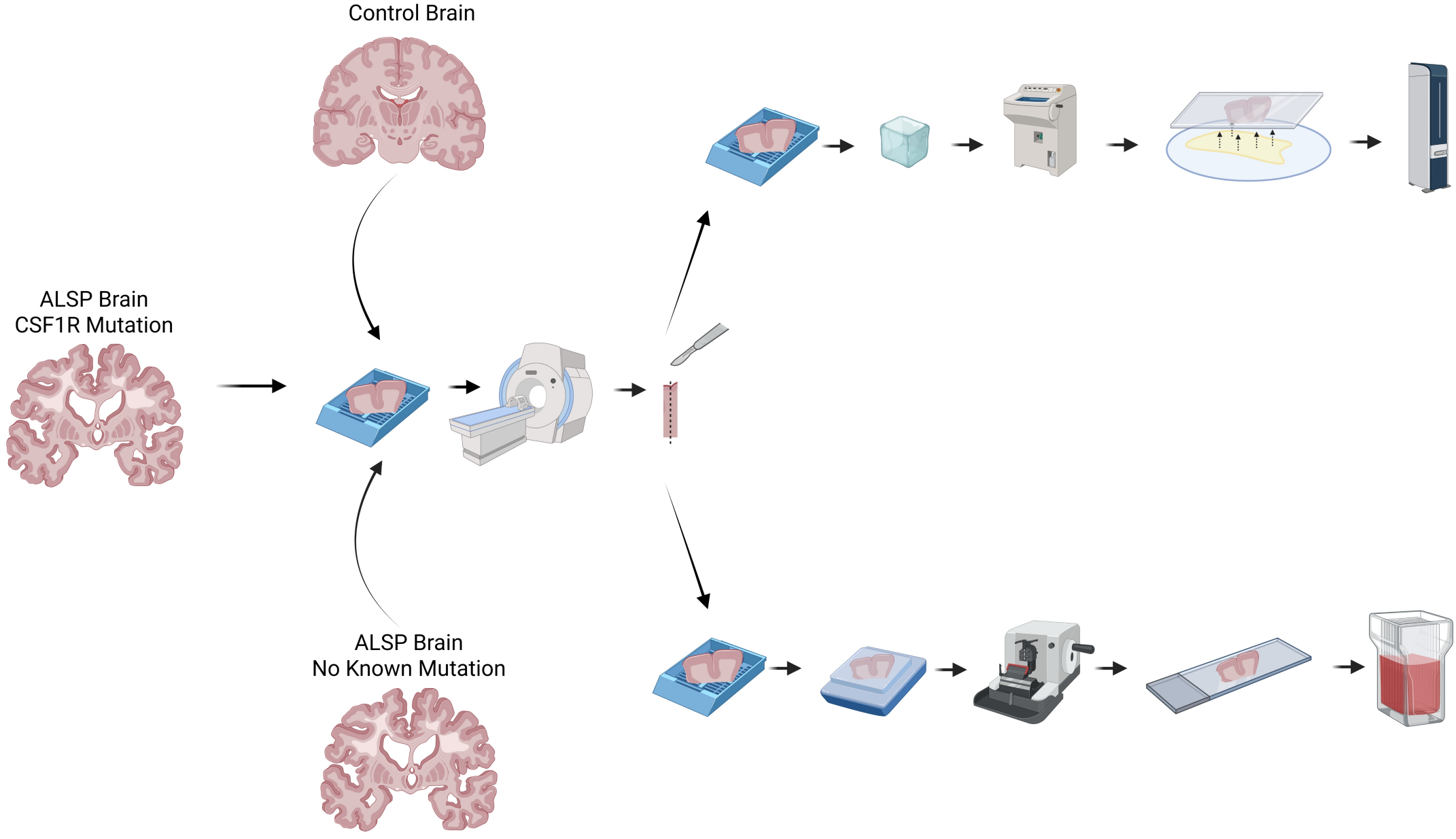
Control Brain
ALSP Brain
CSF1R Mutation
ALSP Brain
No Known Mutation

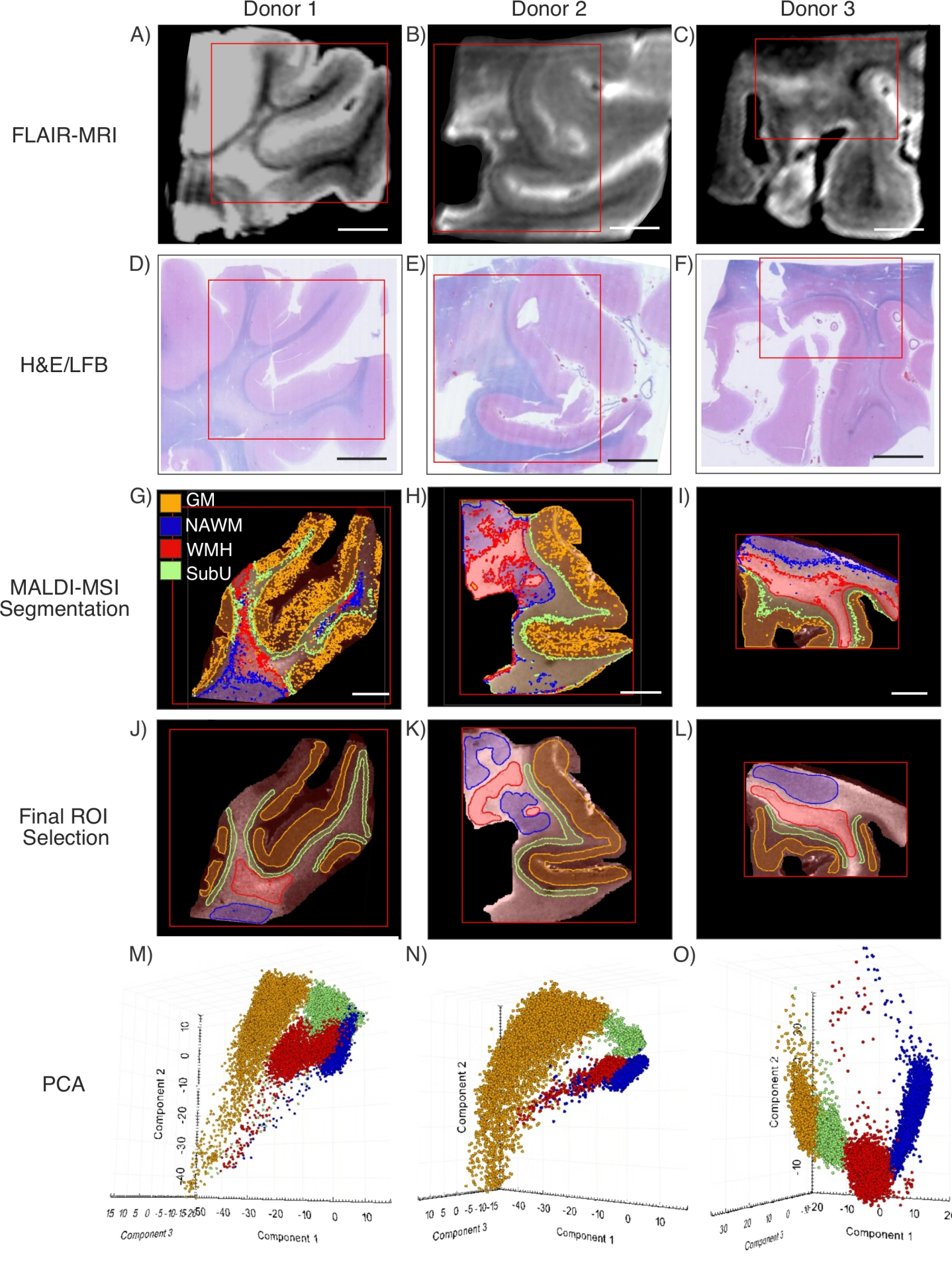
Donor 1
Donor 2
Donor 3
A)
B)
C)
FLAIR-MRI
D)
E)
F)
H&E/LFB
G)
GM
NAWM
WMH
SubU
H)
I)
MALDI-MSI
Segmentation
J)
K)
L)
Final ROI
Selection
M)
N)
O)
PCA
Component 2
Component 3
Component 1

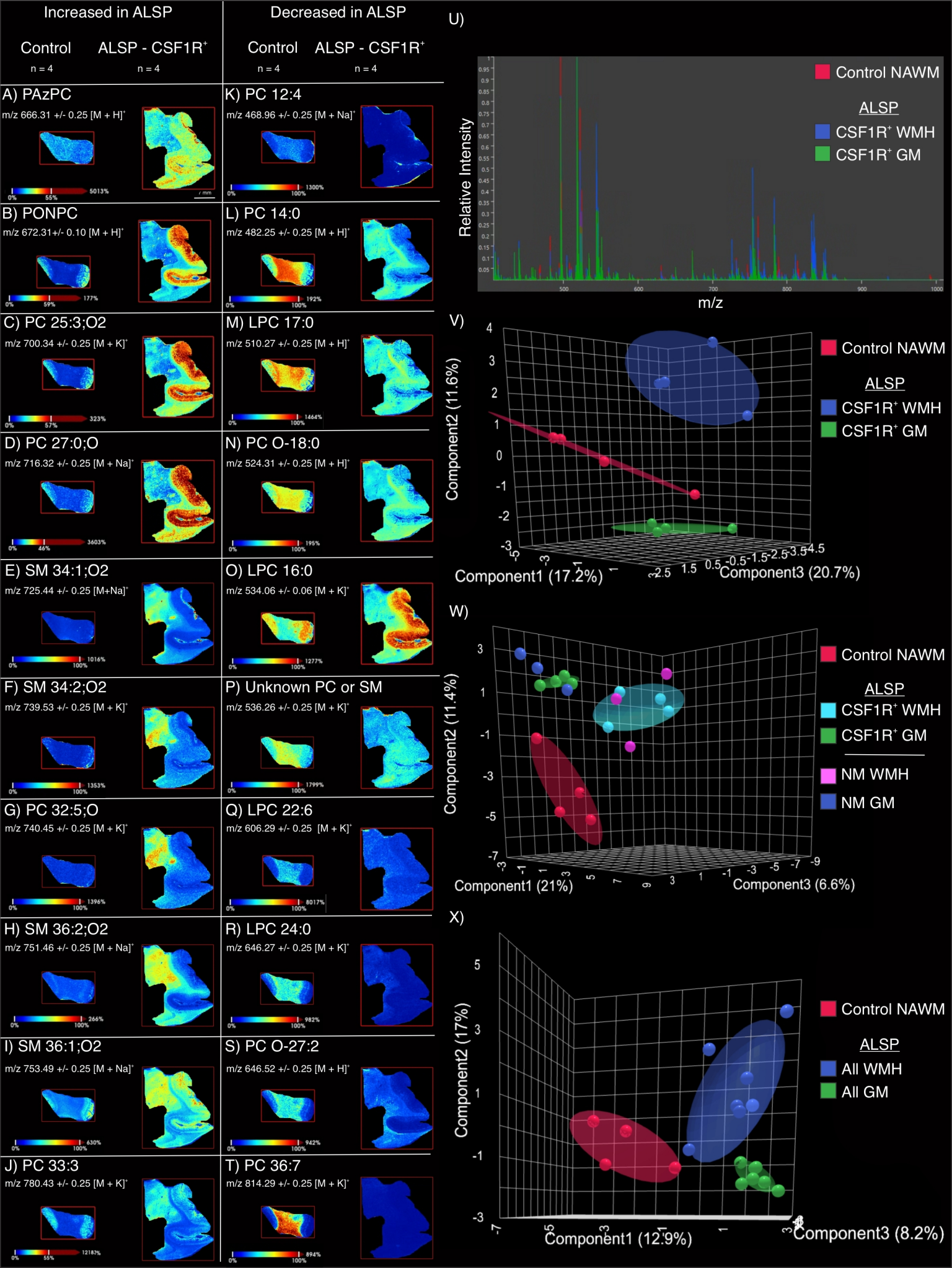
Increased in ALSP
Control
n = 4
ALSP - CSF1R+
n = 4
Decreased in ALSP
Control
n = 4
ALSP - CSF1R+
n = 4
A) PAzPC
m/z 666.31 +/- 0.25 [M + H]+
B) PONPC
m/z 672.31+/- 0.10 [M + H]+
C) PC 25:3;O2
m/z 700.34 +/- 0.25 [M + K]+
D) PC 27:0;O
m/z 716.32 +/- 0.25 [M + Na]+
E) SM 34:1;O2
m/z 725.44 +/- 0.25 [M+Na]+
F) SM 34:2;O2
m/z 739.53 +/- 0.25 [M + K]+
G) PC 32:5;O
m/z 740.45 +/- 0.25 [M + K]+
H) SM 36:2;O2
m/z 751.46 +/- 0.25 [M + Na]+
I) SM 36:1;O2
m/z 753.49 +/- 0.25 [M + Na]+
J) PC 33:3
m/z 780.43 +/- 0.25 [M + K]+
K) PC 12:4
m/z 468.96 +/- 0.25 [M + Na]+
L) PC 14:0
m/z 482.25 +/- 0.25 [M + H]+
M) LPC 17:0
m/z 510.27 +/- 0.25 [M + H]+
N) PC O-18:0
m/z 524.31 +/- 0.25 [M + H]+
O) LPC 16:0
m/z 534.06 +/- 0.06 [M + K]+
P) Unknown PC or SM
m/z 536.26 +/- 0.25 [M + K]+
Q) LPC 22:6
m/z 606.29 +/- 0.25 [M + K]+
R) LPC 24:0
m/z 646.27 +/- 0.25 [M + K]+
S) PC O-27:2
m/z 646.52 +/- 0.25 [M + H]+
T) PC 36:7
m/z 814.29 +/- 0.25 [M + K]+
U)
Relative Intensity
m/z
Control NAWM
ALSP
CSF1R+ WMH
CSF1R+ GM
V)
Component2 (11.6%)
Component1 (17.2%)
Component3 (20.7%)
Control NAWM
ALSP
CSF1R+ WMH
CSF1R+ GM
W)
Component2 (11.4%)
Component1 (21%)
Component3 (6.6%)
Control NAWM
ALSP
CSF1R+ WMH
CSF1R+ GM
NM WMH
NM GM
X)
Component2 (17%)
Component1 (12.9%)
Component3 (8.2%)
Control NAWM
ALSP
All WMH
All GM

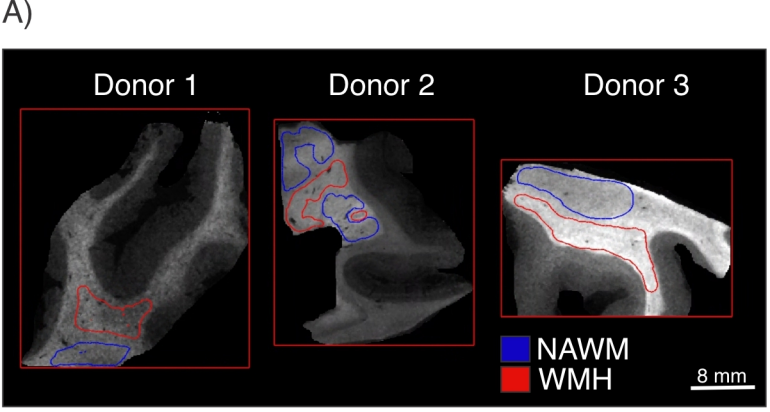
A)
Donor 1
Donor 2
Donor 3
NAWM
WMH
8 mm

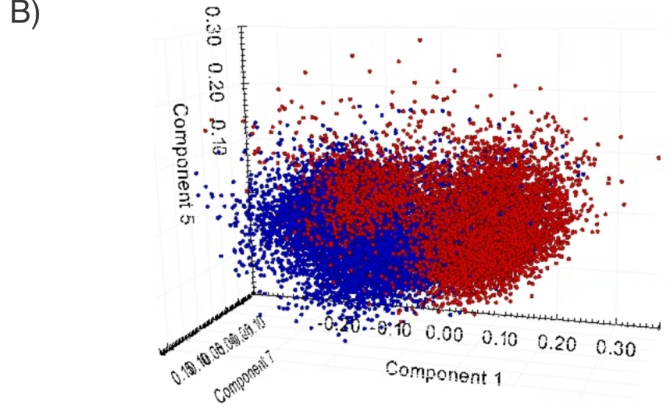
B)
Component 5
Component 1
Component 1

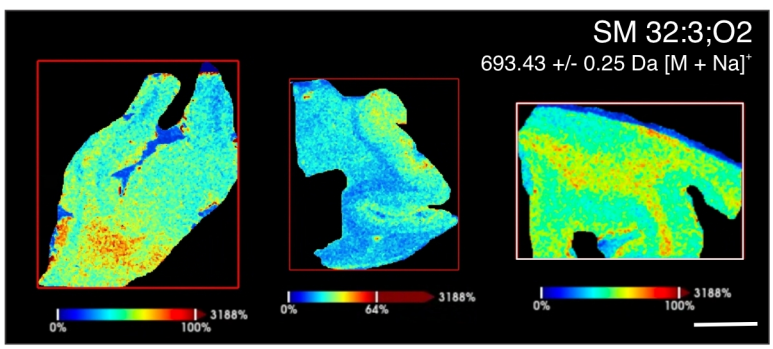
C)
SM 32:3;O2
693.43 +/- 0.25 Da [M + Na]+
0%
100%
3188%
0%
64%
3188%
0%
100%
3188%

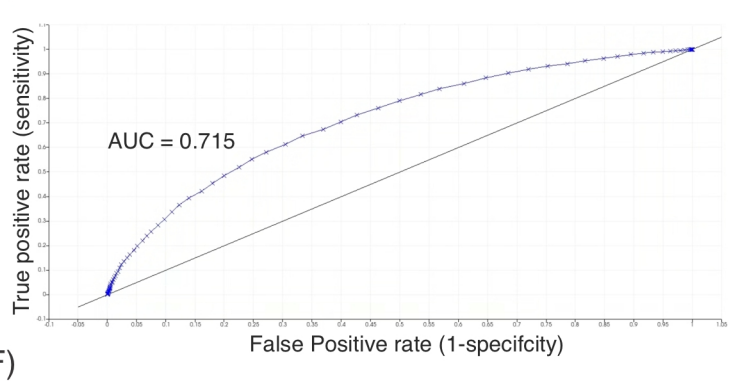
D)
AUC = 0.715
True positive rate (sensitivity)
False Positive rate (1-specifcity)

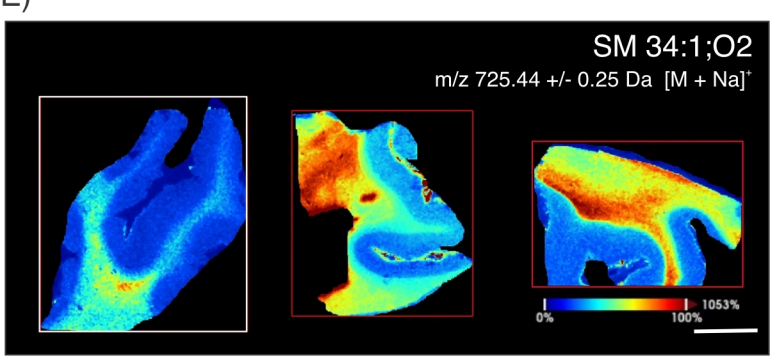
E)
SM 34:1;O2
m/z 725.44 +/- 0.25 Da [M + Na]+
0%
100%
1053%

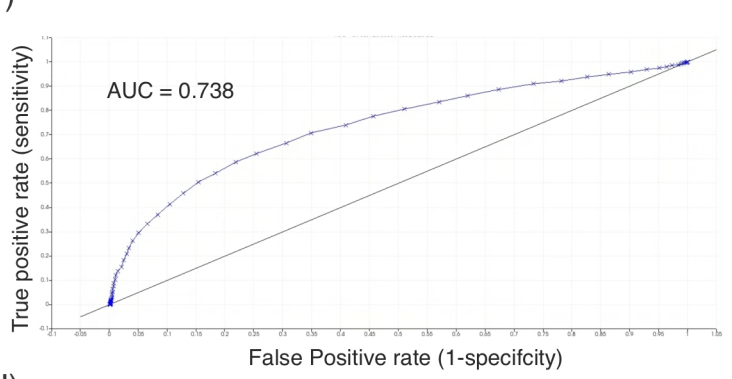
F)
AUC = 0.738
True positive rate (sensitivity)
False Positive rate (1-specifcity)

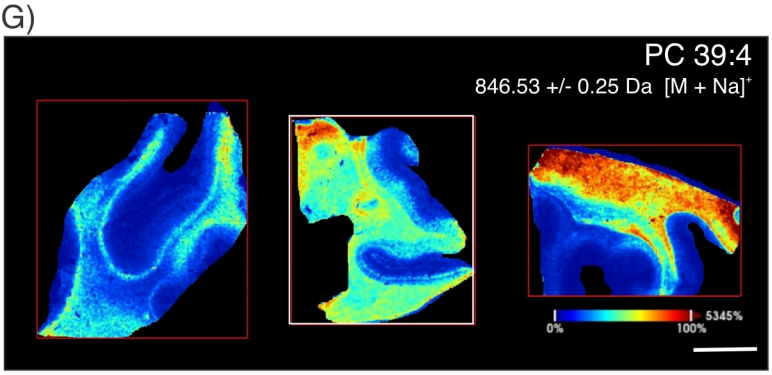
G)
PC 39:4
846.53 +/- 0.25 Da [M + Na]+
0%
100%
5345%

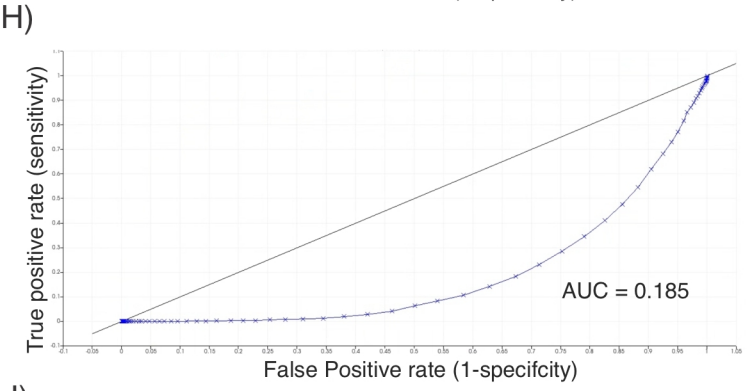
H)
AUC = 0.185
True positive rate (sensitivity)
False Positive rate (1-specifcity)

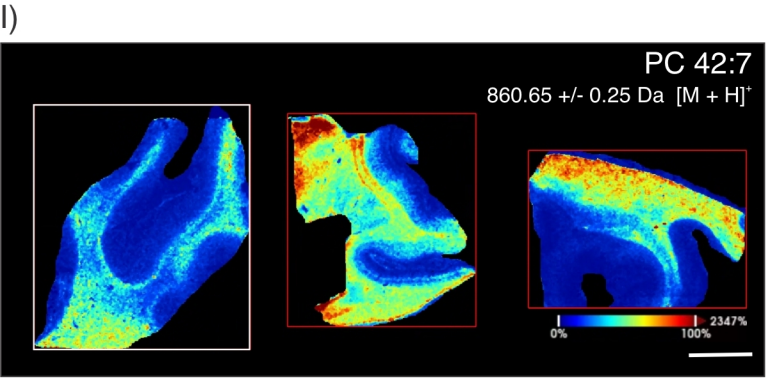
I)
PC 42:7
860.65 +/- 0.25 Da [M + H]+
0%
100%
2347%

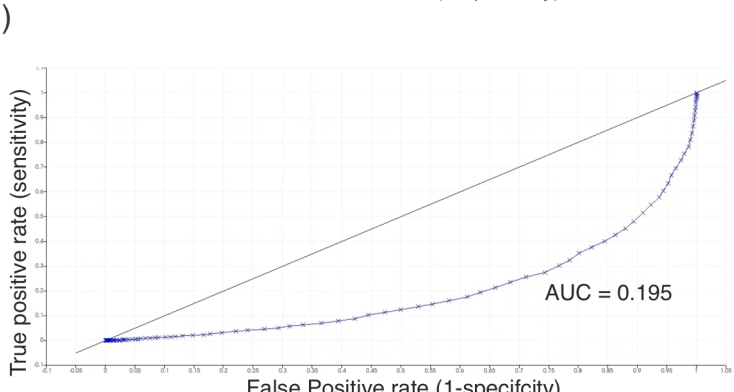
J)
AUC = 0.195
True positive rate (sensitivity)
False Positive rate (1-specifcity)

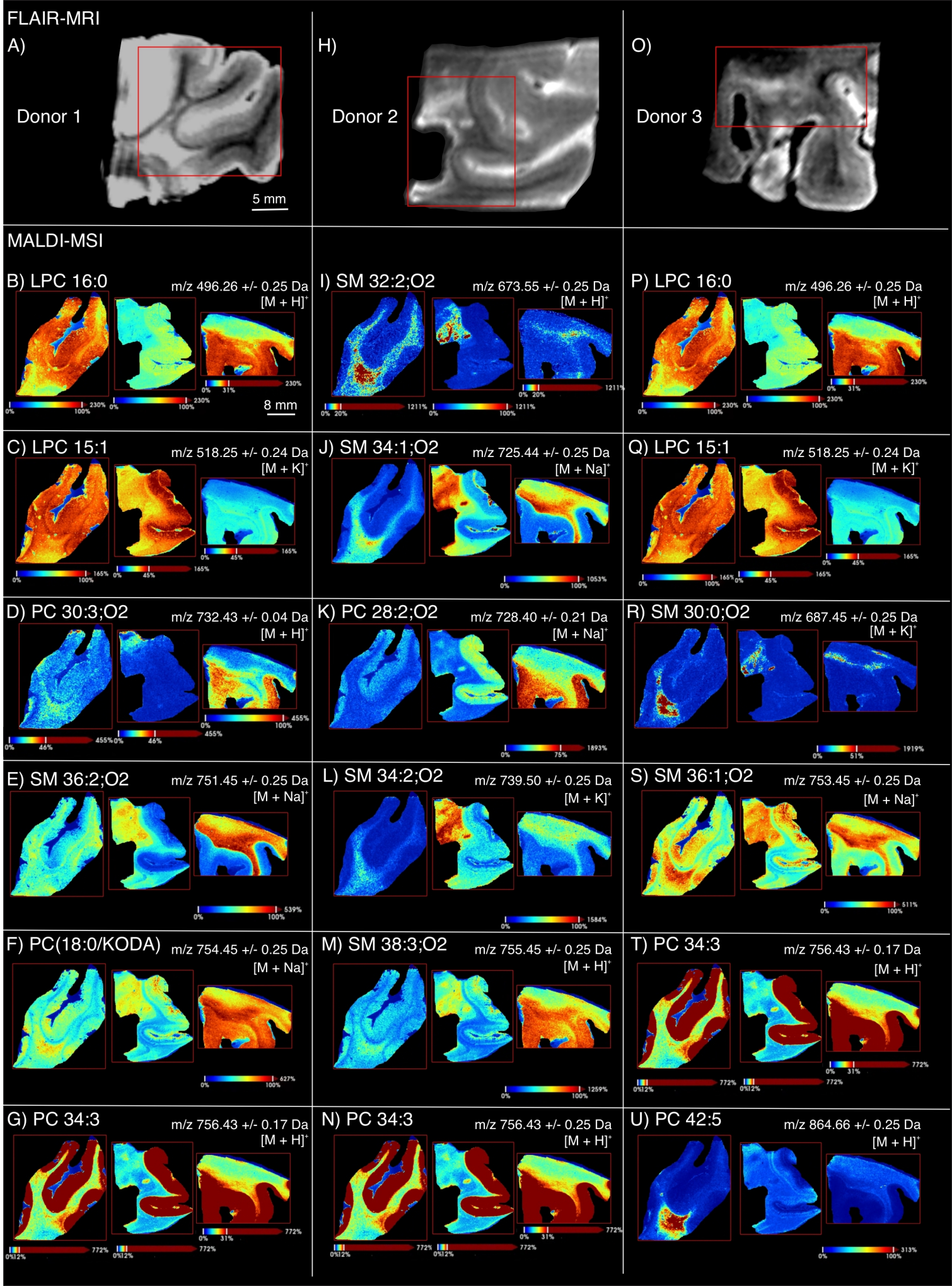
FLAIR-MRI
A)
Donor 1
5 mm
H)
Donor 2
O)
Donor 3
MALDI-MSI
B) LPC 16:0
m/z 496.26 +/- 0.25 Da
[M + H]+
8 mm
I) SM 32:2;O2
m/z 673.55 +/- 0.25 Da
[M + H]+
P) LPC 16:0
m/z 496.26 +/- 0.25 Da
[M + H]+
C) LPC 15:1
m/z 518.25 +/- 0.24 Da
[M + K]+
J) SM 34:1;O2
m/z 725.44 +/- 0.25 Da
[M + Na]+
Q) LPC 15:1
m/z 518.25 +/- 0.24 Da
[M + K]+
D) PC 30:3;O2
m/z 732.43 +/- 0.04 Da
[M + H]+
K) PC 28:2;O2
m/z 728.40 +/- 0.21 Da
[M + Na]+
R) SM 30:0;O2
m/z 687.45 +/- 0.25 Da
[M + K]+
E) SM 36:2;O2
m/z 751.45 +/- 0.25 Da
[M + Na]+
L) SM 34:2;O2
m/z 739.50 +/- 0.25 Da
[M + K]+
S) SM 36:1;O2
m/z 753.45 +/- 0.25 Da
[M + Na]+
F) PC(18:0/KODA)
m/z 754.45 +/- 0.25 Da
[M + Na]+
M) SM 38:3;O2
m/z 755.45 +/- 0.25 Da
[M + H]+
T) PC 34:3
m/z 756.43 +/- 0.17 Da
[M + H]+
G) PC 34:3
m/z 756.43 +/- 0.17 Da
[M + H]+
N) PC 34:3
m/z 756.43 +/- 0.25 Da
[M + H]+
U) PC 42:5
m/z 864.66 +/- 0.25 Da
[M + H]+

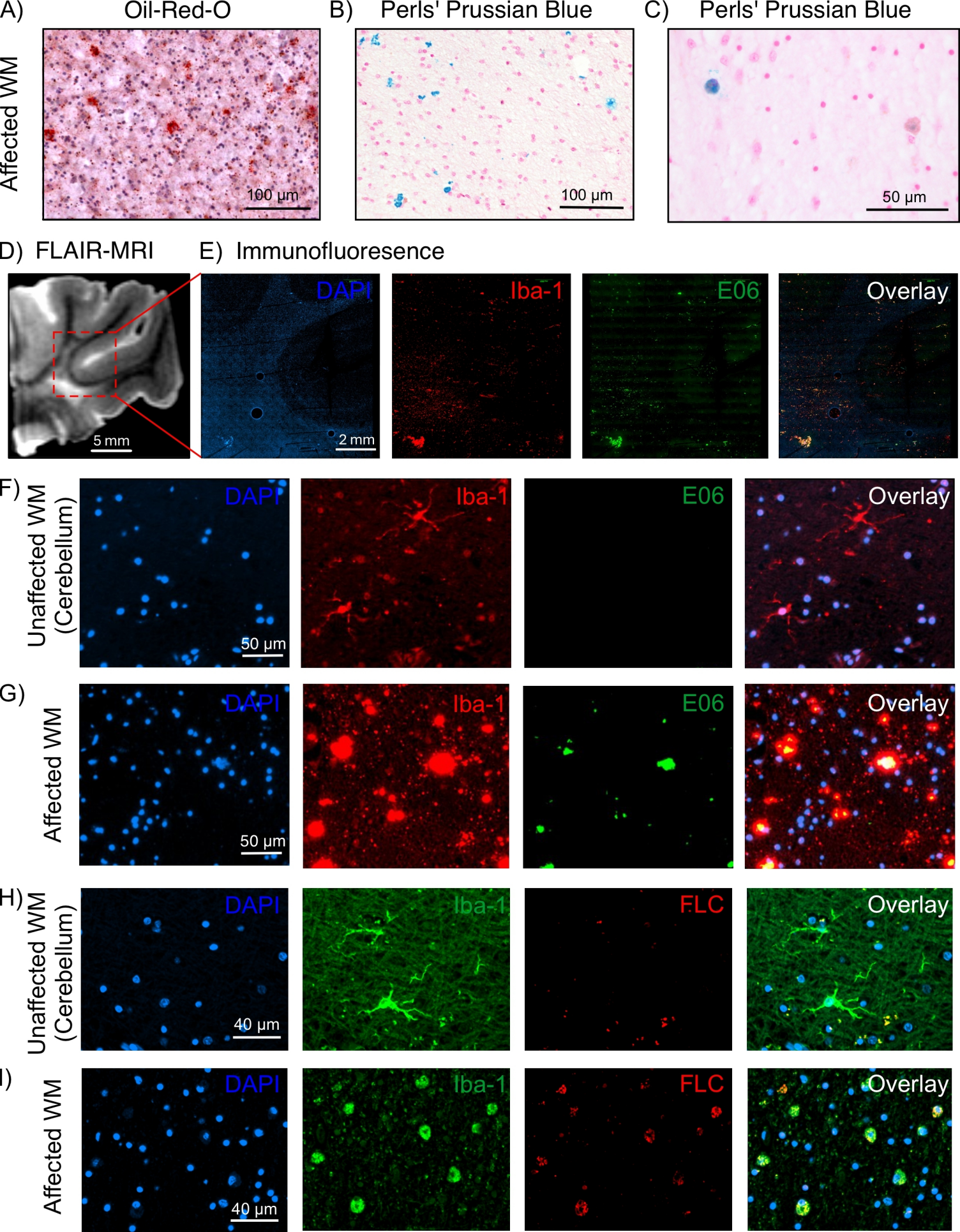
A)
Oil-Red-O
B)
Perls' Prussian Blue
C)
Perls' Prussian Blue
Affected WM
100 µm
100 µm
50 µm
D) FLAIR-MRI
E) Immunofluoresence
5 mm
DAPI
2 mm
Iba-1
E06
Overlay
F)
Unaffected WM (Cerebellum)
DAPI
50 µm
Iba-1
E06
Overlay
G)
Affected WM
DAPI
50 µm
Iba-1
E06
Overlay
H)
Unaffected WM (Cerebellum)
DAPI
40 µm
Iba-1
FLC
Overlay
I)
Affected WM
DAPI
40 µm
Iba-1
FLC
Overlay

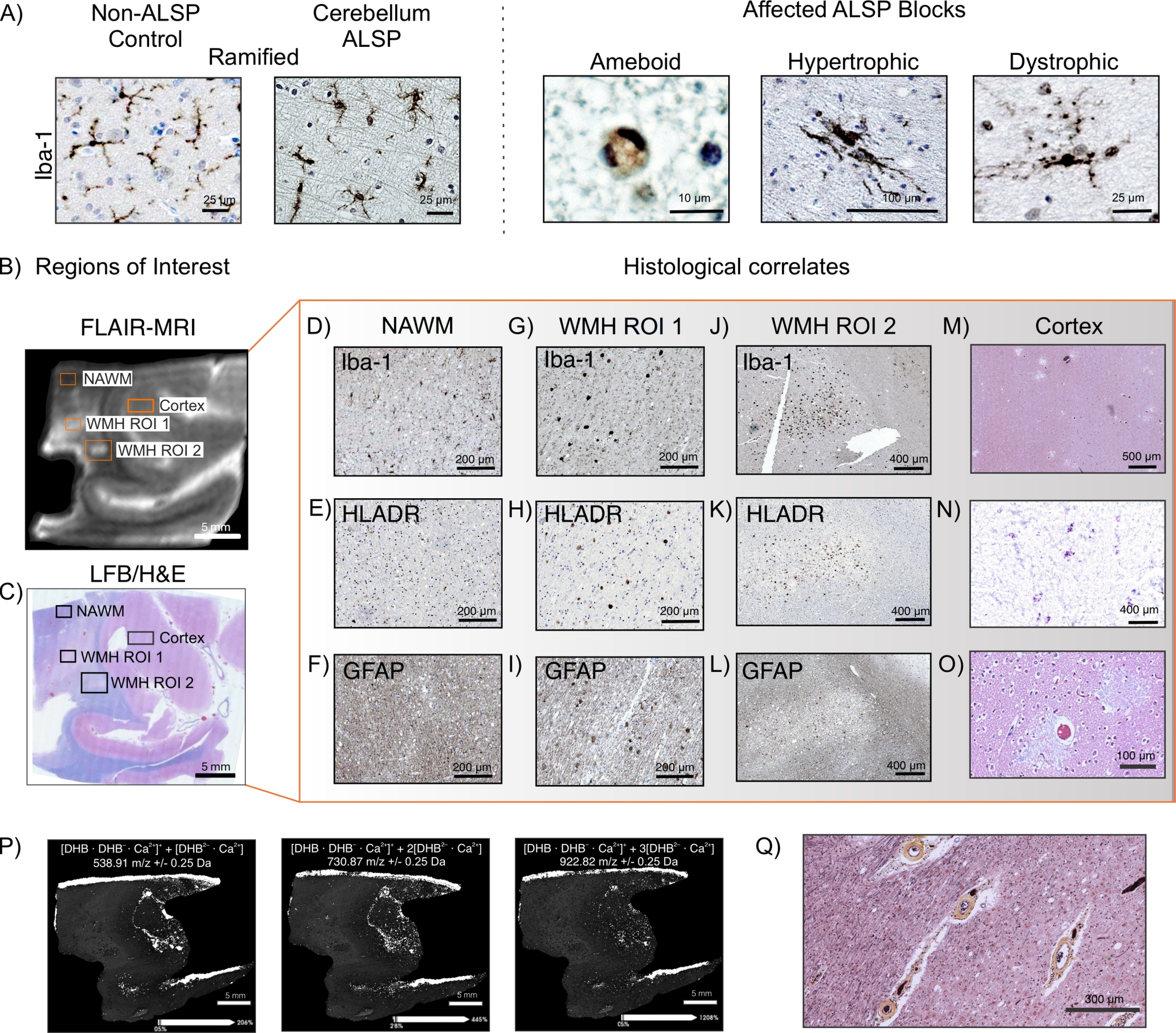
A)
Non-ALSP Control
Cerebellum ALSP
Ramified
Affected ALSP Blocks
Ameboid
Hypertrophic
Dystrophic
Iba-1
25 µm
25 µm
10 µm
100 µm
25 µm
B) Regions of Interest
Histological correlates
FLAIR-MRI
NAWM
Cortex
WMH ROI 1
WMH ROI 2
5 mm
C)
LFB/H&E
NAWM
Cortex
WMH ROI 1
WMH ROI 2
5 mm
D) NAWM
G) WMH ROI 1
J) WMH ROI 2
M) Cortex
Iba-1
200 µm
200 µm
400 µm
500 µm
E) HLADR
H) HLADR
K) HLADR
N)
200 µm
200 µm
400 µm
400 µm
F) GFAP
I) GFAP
L) GFAP
O)
200 µm
200 µm
400 µm
100 µm
P)
[DHB · DHB⁻ · Ca²⁺]⁺ + [DHB²⁻ · Ca²⁺]
538.91 m/z +/- 0.25 Da
[DHB · DHB⁻ · Ca²⁺]⁺ + 2[DHB²⁻ · Ca²⁺]
730.87 m/z +/- 0.25 Da
[DHB · DHB⁻ · Ca²⁺]⁺ + 3[DHB²⁻ · Ca²⁺]
922.82 m/z +/- 0.25 Da
5 mm
5 mm
5 mm
Q)
300 µm

Supplementary Files

This is a list of supplementary files associated with this preprint. Click to download.

- Table1.docx
- Table2.docx
- Table3.docx
- Table4.docx